

# Exchange flow between open water and floating vegetation

Xueyan Zhang · Heidi M. Nepf

Received: 8 July 2010 / Accepted: 17 May 2011 / Published online: 8 June 2011  
© Springer Science+Business Media B.V. 2011

**Abstract** This study describes the exchange flow between a region with open water and a region with a partial-depth porous obstruction, which represents the thermally-driven exchange that occurs between open water and floating vegetation. The partial-depth porous obstruction represents the root layer, which does not penetrate to the bed. Initially, a vertical wall separates the two regions, with fluid of higher density in the obstructed region and fluid of lower density in the open region. This density difference represents the influence of differential solar heating due to shading by the vegetation. For a range of root density and root depths, the velocity distribution is measured in the lab using PIV. When the vertical wall is removed, the less dense water flows into the obstructed region at the surface. This surface flow bifurcates into two layers, one flowing directly through the root layer and one flowing beneath the root layer. A flow directed out of the vegetated region occurs at the bed. A model is developed that predicts the flow rates within each layer based on energy considerations. The experiments and model together suggest that at time- and length-scales relevant to the field, the flow structure for any root layer porosity approaches that of a fully blocked layer, for which the exchange flow occurs only beneath the root layer.

**Keywords** Exchange flow · Vegetation · Lakes · Density-driven exchange · Porous obstruction

## 1 Introduction

Floating vegetation is commonly seen in fresh-water systems, where it can create microenvironments that are chemically distinct from adjacent open water [21]. Floating vegetation also impacts phytoplankton and zooplankton biomass, as well as the predation and habitat of fish communities [2, 12, 15]. In this paper, we consider the role of floating vegetation in

---

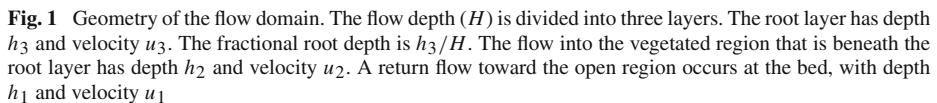
X. Zhang · H. M. Nepf (✉)  
Department of Civil and Environmental Engineering, Massachusetts Institute of Technology,  
Cambridge, MA, USA  
e-mail: hmnepf@mit.edu

the generation of convective water exchange, which may transport water between the chemically distinct regions of open and vegetated water. When solar radiation impinges on an open water surface, the water absorbs solar energy and its temperature increases. In regions with floating vegetation, however, the surface leaves intercept the solar radiation and shade the water column. The difference between the absorption of solar radiation by water in open and vegetated regions creates a difference in water temperature. Ultsch [21] reported temperature as much as 2°C lower beneath water hyacinths than at the same depth in adjacent open water. Similarly, the daytime water temperature within the marsh region of a constructed wetland remained 2°C cooler than the open pond area [10]. These temperature differences produce gradients in density that can drive exchange flows between the open water and the region of vegetation. Lovstedt and Bengtsson [11] measured temperature differences up to 1°C between a reed belt and adjacent open water, and they verified the existence of an exchange flow with velocity up to 1.5 cm/s. For a water body that is sheltered from wind, convective exchange flow of this magnitude will dominate the mass exchange between the vegetated area and the open water [24]. Floating vegetation in particular tends to live in quiescent regions, where background flow conditions are relatively calm [3], so that flow driven by differential shading will likely be important.

In addition to causing an uneven distribution of thermal radiation, the presence of aquatic vegetation also adds hydrodynamic drag. Zhang and Nepf [24] studied the impact of rooted, emergent vegetation on thermally-driven exchange, and they showed that the flow magnitude was controlled by the vegetative drag. Lovstedt and Bengtsson [11] also considered rooted emergent vegetation. In contrast, this paper considers floating vegetation, for which the root layer extends through only a fraction of the water depth, creating an uneven distribution of drag, which should alter the vertical structure of the flow. For example, Coates and Ferris [6] created a thermally-driven exchange between a region with floating *Azolla* and *Lemna* plants and a region of open water. The exchange flow was displaced downward beneath the root layer, which was 2–3 cm thick, with very little flow within the root layer. More recently, [16] studied the adjustment of ocean current near a suspended aquaculture canopy, which occupied a fraction of the water depth. The strength of the stratification and the horizontal span of the canopy determined whether the incoming flow was diverted downward beneath the canopy or horizontally around it. In this work, we examine how a root layer changes the vertical distribution of an exchange flow and influences the volume of exchange. In the next section, we use energy conservation to develop a model that predicts the magnitude of exchange. Section 3 describes the experiment. The comparison between theoretical and experimental results, as well as the extension to field conditions, is presented in Sect. 4.

## 2 Model development

Coates and Patterson [7] studied thermally-driven exchange between a shaded and unshaded region of open water without vegetation. Zhang and Nepf [24] studied thermally-driven exchange generated by differential light absorption between a region of open water and a region of emergent, rooted vegetation. In both cases, the distribution of light absorption over depth, which follows Beer's Law, produced vertical variation in temperature, and thus density, in the heated region. Despite this vertical stratification, the exchange flow resulting from the horizontal density difference consisted of a single intrusion and a single return flow at the bed. That is, the presence of stratification within the intrusion had no observable influence on the layer structure. Given these observations, we believe that a lock exchange, with an



The geometry of the lock exchange model is depicted in Fig. 1. We consider a rectangular flow domain with a total depth  $H$  and a total length  $2L_{tank} \gg H$  (the figure is not to scale). A removable gate is located at  $x = 0$ . Initially, the water to the right of the gate has a higher density than the water to the left of the gate. In the lab, we use salt to change the water density, and so we label the two densities,  $\rho_s$  (saltwater) and  $\rho_f$  (fresh water), shown in white and grey, respectively, in Fig. 1. Floating vegetation is present to the right of the gate, and the root depth is  $h_3$ . The fractional root depth is  $h_3/H$ . In the lab, the root layer is modeled by an array of circular cylinders with diameter  $d$ . The root density is described by the ratio of root volume to total volume,  $\phi$ , called the solid volume fraction, and by the frontal area per unit volume,  $a = Nd/A$ , in which  $N$  is the number of roots per planar area  $A$ .

The exchange flow is initiated when the gate is removed. The surface current is broken into two layers, flow through the root layer and flow beneath the roots, in a layer of depth  $h_2$ . The return current at the bed has depth  $h_1$ . The velocity of each layer is given by  $u_j$ ,  $j = 1, 2, 3$ . The extension of each layer beyond the initial position,  $x = 0$ , is denoted  $L_1$ ,  $L_2$  and  $L_3$ , respectively.

$$D = \frac{1}{\gamma} C_D a \rho_f u_3^2 h_3 L_3 \quad (1)$$
$$u_2 h_2 + u_3 h_3 = u_1 h_1 \quad (2)$$

and

$$h_1 + h_2 + h_3 = H \quad (3)$$

The roots exert a drag that retards flow, so that the velocity within the root layer is expected to be lower than the velocity beneath the root layer. We characterize this difference with this velocity ratio.

$$\alpha = u_3/u_2 \quad (4)$$

where  $\alpha$  is smaller than 1. With the following simplifying assumptions, we can estimate  $\alpha$  from the equations of linear momentum. First, when vegetation is present, the viscous drag is negligible compared to the vegetative drag [20, 23]. Second, initially the exchange flow is dominated by inertia (following the classic evolution), but within the root layer the vegetative drag exceeds inertia for  $C_{Da}L_3 > 7$  [20]. The initial inertia-dominated regime is discussed in the results, but here we consider only the drag-dominated limit, so that within the root layer the inertia term is negligible compared to the drag term. Finally, we assume that the flow is slowly varying, so that a steady approximation can be made. For two-dimensional, steady flow we then have the following equations of momentum,

$$0 = -\frac{\partial P_3}{\partial x} - \frac{1}{2}\rho_f C_{Da}u_3^2 \quad \text{root layer} \quad (5)$$

$$\rho_f u_2 \frac{\partial u_2}{\partial x} = -\frac{\partial P_2}{\partial x} \quad \text{layer beneath roots} \quad (6)$$

The longitudinal gradients in pressure and velocity occur over the length-scale of the exchange flow, which we represent by  $L = L_2$ , since  $L_2 > L_3$  (Fig. 1), so that  $\partial x \sim L$ . Therefore, we write  $\partial u_2/\partial x \sim u_2/L$ . In addition, the pressure gradient acting on both layers depends on the density difference between the two reservoirs, and thus has the same scale in the two layers, i.e.  $\partial P_2/\partial x = \partial P_3/\partial x \approx (\rho_s - \rho_f)gH/L$ . With these scales, Eqs. 5 and 6 can be combined to yield,

$$\frac{u_2^2}{L} \sim \frac{1}{2}C_{Da}u_3^2 \quad (7)$$

From Eq. 7, the velocity ratio is

$$\alpha = u_3/u_2 = K \left( \frac{2}{C_{Da}L} \right)^{1/2} \quad (8)$$

This represents the ratio of the drag-dominated velocity scale to the inertial velocity scale. The scale constant  $K$  will be determined by experiment.

The total energy in the system is the sum of potential (PE) and kinetic (KE) energy. Over time, energy is lost to dissipation in the root layer. This dissipation is equivalent to the rate of work done against the root-layer drag, i.e.  $Du_3$ . The rate of change of the total energy in the system is then,

$$\frac{\partial KE}{\partial t} + \frac{\partial PE}{\partial t} = -Du_3 \quad (9)$$

The potential (PE) and kinetic (KE) energy per unit width are given by the following equations. For simplification, we use  $\Delta\rho = \rho_s - \rho_f$ .

$$PE = \frac{1}{2}\rho_f g H^2 L_{\text{tank}} + \frac{1}{2}\rho_s g H^2 L_{\text{tank}} + \frac{1}{2}\Delta\rho g L_1 h_1^2 - \Delta\rho g L_3 h_3 \left(H - \frac{h_3}{2}\right) - \Delta\rho g L_2 h_2 \left(H - h_3 - \frac{h_2}{2}\right) \quad (10)$$

$$KE = \frac{1}{2}\rho_s u_1^2 h_1 (L_1 + L_2) + \frac{1}{2}\rho_f (u_2^2 h_2 L_2 + u_3^2 h_3 L_3) + \frac{1}{2}\rho_f \left(\frac{u_1 h_1}{h_2 + h_3}\right)^2 (h_2 + h_3) L_1 \quad (11)$$

The last term in Eq. 11 represents flow in the open region of the upper layer (Fig. 1), which supplies flow into the vegetated region. The velocity in this area is assumed to be uniform and from continuity must have the magnitude  $u_1 h_1 / (h_2 + h_3)$ .

Differentiating Eqs. 10 and 11 with respect to time, gives the rate of change in potential and kinetic energy,  $\partial PE / \partial t$  and  $\partial KE / \partial t$ , per unit width, respectively. We use the fact that  $u_j = \partial L_j / \partial t$ . We also assume  $\partial u_j / \partial t \approx 0$ , which is justified based on experimental observations. Note that the first two terms in (10) are not functions of time, and we assume the layer depths are also constant, so that the rate of change in potential energy is

$$\frac{\partial PE}{\partial t} = \frac{1}{2}\Delta\rho g u_1 h_1^2 - \Delta\rho g u_3 h_3 \left(H - \frac{h_3}{2}\right) - \Delta\rho g u_2 h_2 \left(H - h_3 - \frac{h_2}{2}\right) \quad (12)$$

and the rate of change in kinetic energy is

$$\frac{\partial KE}{\partial t} = \frac{1}{2}\rho_s u_1^2 h_1 (u_1 + u_2) + \frac{1}{2}\rho_f (u_2^3 h_2 + u_3^3 h_3) + \frac{1}{2}\rho_f \left(\frac{u_1 h_1}{h_2 + h_3}\right)^2 (h_2 + h_3) u_1 \quad (13)$$

With some algebraic manipulation, Eq. 12 can be written in terms of the inertial velocity,  $u_i$ , for the density-driven exchange flow between two open regions [5],

$$u_i = \frac{1}{2} (g' H)^{1/2} \quad (14)$$

The reduced gravity is  $g' = g \Delta\rho / \rho_s$ . Equation 12 then becomes,

$$\frac{\partial PE}{\partial t} = 2\rho_s u_i^2 u_1 \frac{h_1^2}{H} - 4\rho_s u_i^2 u_3 \frac{h_3}{H} \left(H - \frac{h_3}{2}\right) - 4\rho_s u_i^2 u_2 \frac{h_2}{H} \left(H - h_3 - \frac{h_2}{2}\right) \quad (15)$$

With five unknowns ( $h_1, h_2, u_1, u_2, u_3$ ), but only four equations (Eqs. 2, 3, 8, 9), an additional constraint is needed to find a unique solution. Following previous studies of exchange flow, we set an additional constraint that the system adjusts to maximize the conversion to kinetic energy, or equivalently to maximize the exchange flow rate  $q$ , a condition that has been verified by Jirka [9] and by Adams and Cosler [1]. The exchange flow rate is given by

$$q = u_1 h_1 = u_2 h_2 + u_3 h_3 \quad (16)$$

The equations are made dimensionless by normalizing the layer depths by the total water depth  $H$ , and the velocities by the inertial velocity,  $u_i$ , given in Eq. 14. The non-dimensional terms are denoted by a prime, e.g.  $h'_1 = h_1 / H$  and  $u'_1 = u_1 / u_i$ . The density is normalized

by  $\rho_s$ , and we adopt the Boussinesq approximation,  $\rho_f/\rho_s \approx 1$ . The normalized equations are an optimization problem with the objective function

$$\text{Maximize}(q') \quad (17)$$

subject to

$$\begin{aligned} u'_2 h'_2 + u'_3 h'_3 &= u'_1 h'_1 \\ h'_1 + h'_2 + h'_3 &= 1 \\ \frac{\partial P E'}{\partial t} &= 2u'_1 h_1'^2 - 4u'_3 h'_3 \left(1 - \frac{h'_3}{2}\right) - 4u'_2 h'_2 \left(1 - h'_3 - \frac{h'_2}{2}\right) \\ \frac{\partial K E'}{\partial t} &= \frac{1}{2} u_1'^2 (u'_1 + u'_2) h'_1 - \frac{1}{2} (u_2'^2 h'_2 + u_3'^2 h'_3) + \frac{1}{2} \frac{(u'_1 h'_1)^2}{h'_2 + h'_3} u'_1 \\ \frac{\partial K E'}{\partial t} + \frac{\partial P E'}{\partial t} &= -\frac{1}{2} C_D a L_3 u_3'^3 h'_3 \\ \frac{u'_3}{u'_2} &= K \left(\frac{2}{C_D a L}\right)^{1/2} \end{aligned} \quad (18)$$

The normalized solution has no dependence on the density difference  $\Delta\rho$  or the reduced gravity  $g'$ . Note that the total domain length  $L_{\text{tank}}$  also drops out of the formulation, so that the result is not dependent on the flow domain, as expected. Finally, if we let  $a = 0$ , or  $h_3 = 0$ , we recover the classic solution without vegetation or dissipation, namely,  $u_1 = u_2 = 0.5(g'H)^{1/2}$ .

### 3 Experimental procedures

Experiments were conducted in a Plexiglass<sup>®</sup> tank with the following dimensions: 200 cm(L)  $\times$  12.0 cm(W)  $\times$  20.0 cm(H). A schematic of the tank is shown in Fig. 2. The tank had two chambers of equal size, separated by a vertical removable gate. The chambers were filled to depth  $H = 15$  cm with fresh water (left side) and salt water (right side). The density of water in each chamber was measured by hydrometer.

As the experiments focused on the impact of the root depth and stem density, the water density difference was kept approximately constant across the suite of experiments. We chose a density difference based on Froude number similarity to the field. Lightbody et al. [10] and Ultsch [21] report a temperature difference of 2°C between open water and water beneath vegetation, which corresponds to  $\Delta\rho = 0.0005 \text{ g cm}^{-3}$ . In the field,  $H = 10$  cm to 1 m in vegetated regions, so the velocity-scale  $(g'H)^{1/2}$  is  $O(1 \text{ cm/s})$ . This is consistent with the field observations of velocity made by Lovstedt and Bengtsson [11]. We choose  $\Delta\rho$  to produce a similar velocity scale in the lab. In the field the Reynolds number,  $Re = UH/\nu$ , is  $O(10^3\text{--}10^4)$ . Because our tank is 20 cm deep, we can only match the lower range of  $Re$ . However, previous researchers have shown that the dynamics of gravity currents are described primarily by the Froude number,  $Fr = U/(g'H)^{1/2}$ , with only a small dependence on Reynolds number. Specifically,  $Fr = 0.42$  at  $Re = 200$  and increases to  $Fr = 0.48$  at  $Re = 10^5$ , consistent with a diminished impact of viscosity relative to inertia [4]. Since we cannot match both dimensionless parameters, we follow a Froude number scaling, consistent with previous studies in gravity currents (e.g. [18] and references therein).

A PVC board with a random distribution of holes covered the right side of the tank. Dowels with diameter  $d = 0.6$  cm were pushed through holes to create a root layer of desired

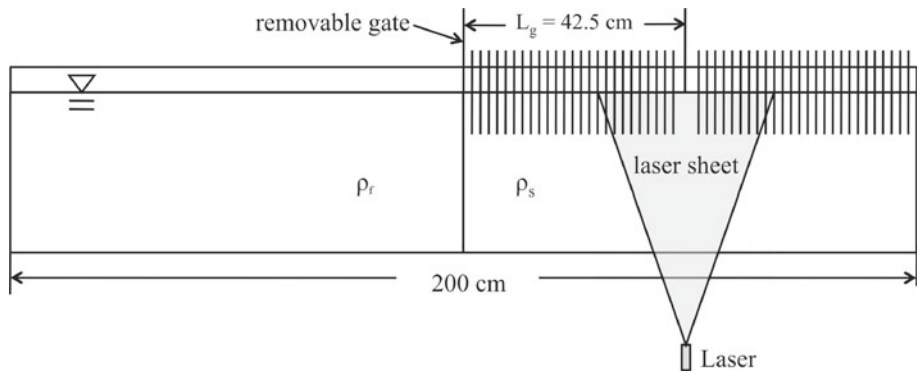


**Fig. 2** A sketch of the experimental setup. Initially, a reservoir of salt water ( $\rho_s$ ) and a reservoir of fresh water ( $\rho_f$ ) are separated by a removable gate. A 5-cm gap in the root layer allows PIV imaging within the root layer. The middle of the gap is located  $L_g = 42$  cm from the gate. Not to scale

depth. Two fractional root depths were considered,  $h_3/H = 0.13$  and  $0.27$ . In the field, root depth,  $h_3$ , ranges from 10 to 80 cm, and fractional root depth is roughly  $h_3/H = 0.1$ – $0.8$  (M. Downing-Kunz, pers. comm.). Each hole on the board was assigned a number, and a program was used to select a random subset of holes to create the desired root density, or solid volume fraction. We considered five solid volume fractions between  $\phi = 0.05$  ( $a = 6.4 \text{ m}^{-1}$ ) and  $\phi = 0.15$  ( $a = 31.8 \text{ m}^{-1}$ ). In the field,  $\phi$  ranges from 0.01 for water lily to 0.45 for mangroves [13]. The root density for floating vegetation has not been reported in the literature, but is expected to fall into a similar range. A difference between the field and the lab model is the scale of individual roots, which are smaller in the field (1–2 mm diameter) than the rods used in the lab (6 mm). This impacts the velocity field at the scale of the roots, but not the bulk behavior of the flow. Specifically, the volumetric discharge, which is the focus of this study, should be comparable for comparable values of dimensionless drag ( $C_D a L$ ), regardless of root diameter. Finally, to explore the limit of a fully blocked root layer, two experiments (S1 and S2 in Table 1) were conducted for  $\phi = 1$ , by replacing the cylinder array with a solid block.

Flow visualization with dye was used to examine the initial inertial response and the subsequent transition to a drag-dominated response. The fresh water was dyed with fluorescein. The vegetated region was illuminated through the tank bottom with an ultraviolet light. A CCD camera was positioned to capture the exchange flow at the middle of the vegetated region. The pictures were taken at 5 fps. After the toe of the intruding current passed the visualization window, a second tracer, crystalline potassium permanganate, was dropped in the middle of the visualization window to generate a vertical streak. The distortion of this streak revealed the shape of the vertical velocity profile at this later time.

Detailed profiles of velocity were acquired using Particle Imaging Velocimetry (PIV). To image the flow in the root layer, it was necessary to create a 5-cm wide gap starting 40 cm from the gate. The distance from the gate to the middle of the gap is denoted  $L_g = 42.5$  cm. The width of the gap was chosen both to reliably calculate the velocity field and to minimize the impact of the gap on the flow inside the root layer. Pliolite particles with a density of  $1.02 \text{ g/cm}^3$  were added to the water. The particle settling velocity was  $O(0.01 \text{ cm/s})$ , which was negligible compared to the exchange flow velocity,  $O(1 \text{ cm/s})$ . The particles were illuminated by a laser sheet that entered through the bottom of the tank (Fig. 2). The movement of the particles was captured using a Sony CCD camera with a resolution of  $1024 \times 768$ .

**Table 1** Summary of experimental parameters

Case uncertainty	$\phi \pm 0.005$	$a(\text{m}^{-1}) \pm 0.1$	$h_3/H \pm 0.01$	$\rho_f(\text{g cm}^{-3})$ $\pm 0.00005$	$\rho_s(\text{g cm}^{-3})$ $\pm 0.00005$
1	0.03	6.4	0.13	0.9980	1.0000
2	0.05	10.6	0.13	0.9985	0.9995
3	0.08	16.9	0.13	0.9990	1.0000
4	0.10	21.2	0.13	0.9975	0.9990
5	0.15	31.8	0.13	0.9985	1.0005
6	0.03	6.4	0.27	0.9985	1.0000
7	0.05	10.6	0.27	0.9985	0.9995
8	0.08	16.9	0.27	0.9975	0.9985
9	0.10	21.2	0.27	0.9975	0.9990
10	0.15	31.8	0.27	0.9985	0.9995
S1	1.0	—	0.13	0.9980	1.0000
S2	1.0	—	0.27	0.9880	1.0000

**Table 2** Summary of experimental results

Case	$u_i(\text{cm s}^{-1})$	$u_1(\text{cm s}^{-1})$	$u_2(\text{cm s}^{-1})$	$u_3(\text{cm s}^{-1})$	$h_2(\text{cm})$	$C_D \pm 10\%$
1	$2.7 \pm 0.5$	$1.8 \pm 0.3$	$2.6 \pm 0.3$	$1.5 \pm 0.2$	$5.0 \pm 0.4$	5.8
2	$1.9 \pm 0.7$	$1.7 \pm 0.2$	$3.0 \pm 0.4$	$0.9 \pm 0.3$	$4.5 \pm 0.3$	11
3	$1.9 \pm 0.7$	$1.8 \pm 0.3$	$2.5 \pm 0.4$	$0.5 \pm 0.3$	$5.6 \pm 0.4$	21
4	$2.3 \pm 0.6$	$2.1 \pm 0.2$	$3.2 \pm 0.4$	$0.5 \pm 0.3$	$5.0 \pm 0.3$	32
5	$2.7 \pm 0.5$	$2.6 \pm 0.3$	$2.8 \pm 0.4$	$0.8 \pm 0.5$	$5.9 \pm 0.7$	50
6	$2.3 \pm 0.6$	$1.4 \pm 0.2$	$2.3 \pm 0.3$	$1.5 \pm 0.2$	$2.5 \pm 0.2$	5.8
7	$1.9 \pm 1.0$	$1.5 \pm 0.2$	$2.1 \pm 0.4$	$0.4 \pm 0.3$	$3.6 \pm 0.6$	12
8	$1.9 \pm 0.7$	$1.7 \pm 0.2$	$2.7 \pm 0.3$	$0.5 \pm 0.3$	$3.8 \pm 0.6$	19
9	$2.3 \pm 0.6$	$1.9 \pm 0.3$	$2.8 \pm 0.4$	$0.8 \pm 0.3$	$3.8 \pm 0.6$	26
10	$1.9 \pm 0.7$	$1.5 \pm 0.3$	$2.5 \pm 0.6$	$0.10 \pm 0.10$	$5.2 \pm 0.8$	66
S1	$2.7 \pm 0.5$	$2.0 \pm 0.2$	$1.5 \pm 0.2$	—	$5.0 \pm 1.0$	—
S2	$2.7 \pm 0.5$	$2.0 \pm 0.2$	$2.5 \pm 0.2$	—	$4.5 \pm 0.4$	—

at a frame rate of 5 fps. The image acquisition was started after the intrusion passed the imaging window, so that the start time was different for each case. The images obtained were processed by MatPIVv.161 to produce a velocity field. For each case, a 10 s averaged was constructed from the instantaneous velocity profiles.

The discharge rate was estimated by integrating the velocity profile from the bottom to the point where the flow changes from outflow to inflow. We denote this estimate as  $q_{int}$ . We confirmed that the inflow and outflow agreed, with less than 10% difference, indicating the conservation of volume was satisfied. The velocity profiles were also used to estimate the thicknesses of the layers (Fig. 1). The thickness of the bottom layer,  $h_1$ , was estimated from the height above the bed at which the flow reversed. For example, in Case 2 (Fig. 4),  $h_1 = 8.5 \pm 0.3$  cm. The thickness of layer 2 would then be,  $h_2 = H - h_3 - h_1 = 4.5 \pm 0.3$  cm (Table 2).



The model velocities, defined in Fig. 1, were defined from the measured velocity profiles in the following way. The velocity in the root layer,  $u_3$ , was defined as the average of the velocity over  $h_3$ , the root depth. The velocities in the unobstructed layers ( $u_1, u_2$ ) were defined as the maximum in each layer. The maximum was chosen as the best representation of the velocity in the absence of viscosity, which was neglected in the model. In this way, the choice of  $u_2$  corresponds to the inertial velocity scale defined in the momentum equation, Eq. 6. A second estimate of discharge was then made for comparison to the model. Following from Eq. 16,  $u_1 h_1$  and  $u_2 h_2 + u_3 h_3$  are used as two estimates of model discharge. The mean of the two values was denoted  $q_{16}$ .

Following from (18), each case was classified by the non-dimensional drag parameter,  $C_D a L$  (see also [20]). For simplicity, we let  $L = L_3 = L_g$ , the distance to the center of the visualization window (Fig. 2). Because the velocity measurements were made as the front moved between  $L_g$  and  $2L_g$ , the length  $L_g$  is a reasonable estimate of the length of the intruding current during the velocity measurement. Tanino and Nepf [19] report  $C_D = f(Re_d, \phi)$  for randomly distributed, emergent cylinder arrays. Their semi-empirical relations cover flow conditions  $Re_d = O(1)$  to  $O(100)$  and  $\phi = 0.05$ – $0.4$ , which includes most of the cases we consider. For our case  $\phi = 0.03$ , we estimated  $C_D$  using the empirical equation for an isolated cylinder, as given in White [22, p. 183]. Given the trends of  $C_D$  with  $\phi$ , this is a reasonable approximation [14].

The model prediction (Eqs. 17, 18) required three inputs; the scale coefficient,  $K$ , which was determined by experiment, the fractional root depth,  $h'_3$ , and the non-dimensional drag parameter,  $C_D a L$ . By varying  $h'_3$ , we generated a set of feasible solutions to Eq. 18. From this set, we selected the solution that maximized the total exchange Eq. 17.

## 4 Results

Tanino et al. [20] identified a transition from inertial to drag-dominated flow within an array of cylinders that filled the water depth. They showed that the array drag became dominant over inertia when  $C_D a L > 7$ . We confirmed this transition in partial depth arrays using two modes of flow visualizations (Fig. 3). To visualize the intruding front, the fresh water was dyed with fluorescein. As the front arrived at the visualization region ( $x = 30$ – $55$  cm), the leading edge of the tracer within the root layer was ahead of that in the region beneath the root layer, indicating that up to this time the velocity in the root layer was higher than that beneath the root layer (Fig. 3a). At the time corresponding to Fig. 3a,  $C_D a L_3 = 7$ , indicating that the system had just reached the drag-dominated limit, so that leading up to this time the system had been in the inertial regime. A later time, when the frontal intrusion was longer and  $C_D a L_3 = 18$  is depicted in Fig. 3b. At this point, the system is fully within the drag-dominated regime. The intruding current had a uniform depth, i.e. the interface between the flow in layers 2 and 3 was horizontal, and the velocity in the root layer ( $u_3$ ) was less than the velocity beneath the root layer ( $u_2$ ), consistent with the drag-dominated regime. The new, drag-dominated velocity profile (dashed line, Fig. 3) was revealed by a second tracer (potassium permanganate), whose initial vertical distribution (solid line) was distorted by the flow. The dashed line within the rooted layer represents the velocity profile measured by PIV, scaled to match the dye streak. Note that an unstable vertical density distribution is created at the leading edge, because layer 2 advances ahead of layer 3, carrying lighter fluid beneath denser fluid, e.g. in Fig. 1, the lighter grey layer ( $\rho_f$ ) advances beneath the heavier white layer ( $\rho_s$ ). We suspected that convection will eventually occur at the leading edge of the front, but we were not able to observe it in our tank before the front reached the end

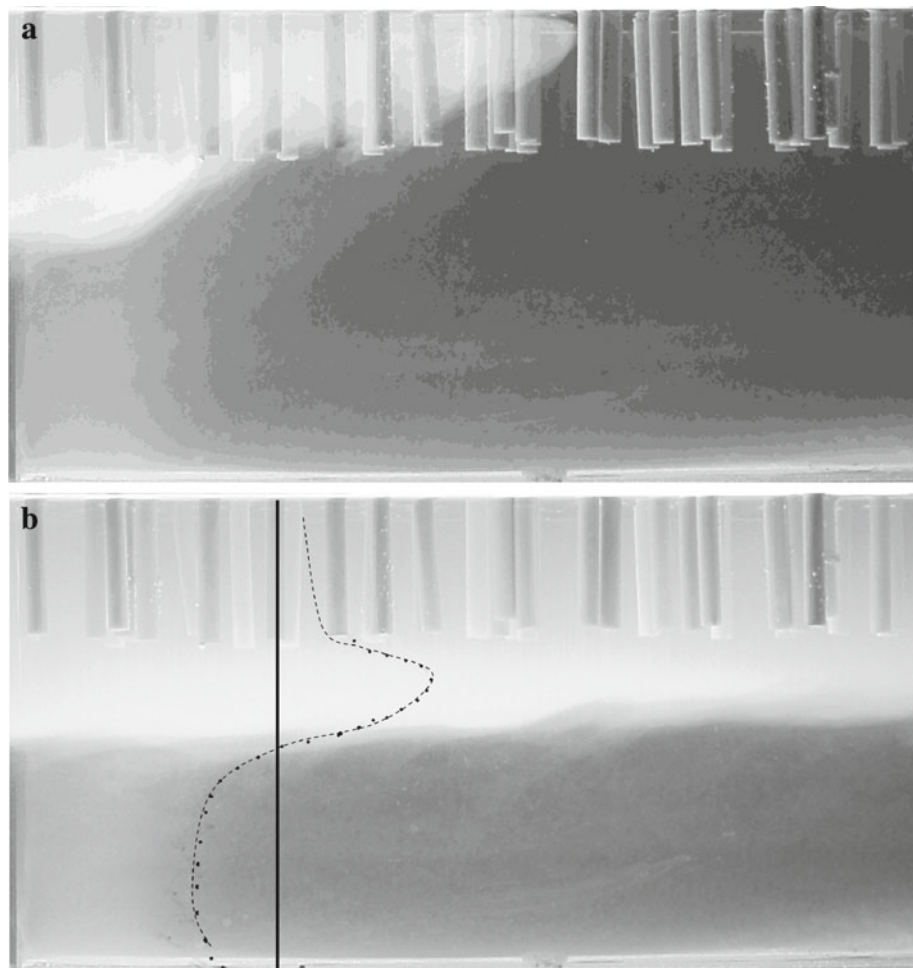


**Fig. 3** Flow visualization using fluorescein and crystalline potassium permanganate. The image corresponds to  $x = 30\text{--}55\text{ cm}$  and  $z = 0\text{--}15\text{ cm}$ . **a** The intruding current arrives 10 s after gate is lifted. The fluid arrives first within the root layer, indicating that up to this point the flow was in the inertial regime. **b** At  $t \approx 30\text{ s}$ , the front is far beyond the visualization window. Crystals of potassium permanganate dropped through the water column creates an initially vertical streak (*solid line*). The distortion of the dye streak (*dotted line*) gives an indication of the velocity field. The dashed line is estimated from PIV measurement, scaled to match the dye streak

wall. Once convection is initiated, the velocities in layers 2 and 3 will be more uniform, as momentum mixes between the layers.

The time-averaged velocity profile for case 2 ( $\phi = 0.05$ ,  $h_3/H = 0.13$ ) is shown in Fig. 4. In this case the root depth,  $h_3$ , is 2 cm. The bottom of the root layer is marked by a horizontal line. The error bars show the standard deviation of the individual measurements made over the 10 sec averaging period. Similarly, the velocity profile for case 7 ( $\phi = 0.05$  with  $h_3/H = 0.28$ ) is shown in Fig. 5. In both cases, the intruding current bifurcated into a distinct flow within the root layer and beneath it, with  $u_3 < u_2$ . The measured values of  $u_2$

**Fig. 4** Time-averaged horizontal velocity profile for case 2 ( $\phi = 0.05$ ,  $h_3/H = 0.13$ ). The bottom of the floating vegetation is at 13 cm, which is marked by a horizontal line. Error bars show the standard deviation of the velocity measurement

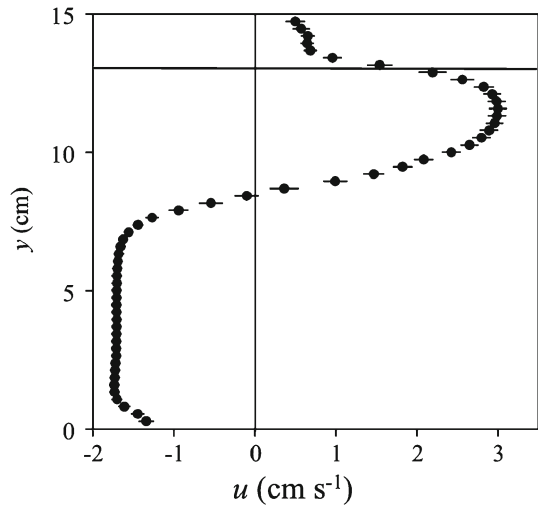
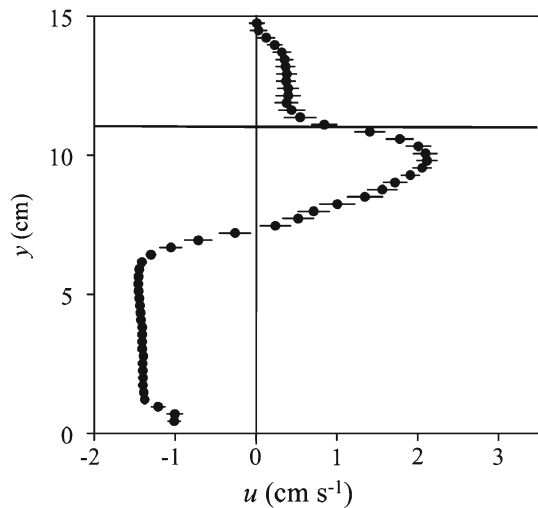


**Fig. 5** Time-averaged horizontal velocity profile for case 7 ( $\phi = 0.05$  with  $h_3/H = 0.28$ ). The bottom of the floating vegetation is at 11 cm, which is marked by a horizontal line. Error bars indicate the standard deviation in the velocity measurement

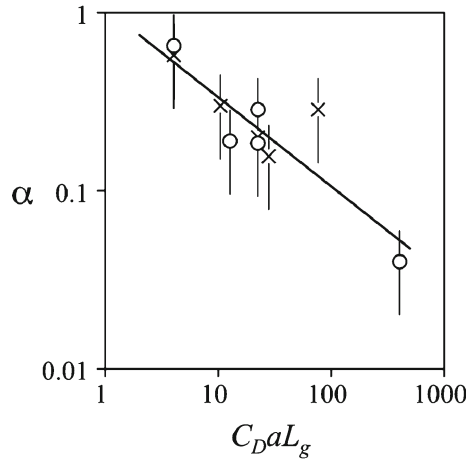


and  $u_3$  for all the cases are listed in Table 2. The uncertainty was estimated by the standard deviation among the 50–60 instantaneous values recorded.

The scale constant,  $K$ , that defines the velocity ratio,  $\alpha = u_3/u_2$  (Eq. 8) was estimated from measured values of  $u_3$  and  $u_2$  (Table 2). The measured  $\alpha$  are plotted against the dimensionless drag,  $C_{Da}L_g$ , and a regression was used to find  $K$  (Fig. 6). The drag coefficient for each case was estimated from empirical relations, as described above, with the values reported in Table 2. The velocity ratio decreases as the dimensionless drag increases, and the trend follows at  $-1/2$  power law, as predicted in Eq. 8. Based on the fit,  $K = 0.75$ .

As  $C_{Da}L$  becomes large, we expect from Eq. 8 and Fig. 6 that the velocity within the root layer will eventually become negligibly small, and the system will behave as if the root layer is fully blocked ( $\phi = 1$ ). To verify this behavior, we compare the velocity profile measured with the highest  $C_{Da}L$  (case 10,  $\phi = 0.15$ ,  $h_3/H = 0.27$ , and  $C_{Da}L = 400$ ) to that measured for a case in which the top layer has the same depth, but is fully blocked (case

**Fig. 6** Velocity ratio  $\alpha$  estimated from measured profiles for cases 1–5 ( $X$ ,  $h_3/H = 0.13$ ) and for cases 6–10 (circle,  $h_3/H = 0.27$ ). The scale constant  $K$  is found by fitting Eq. 8, solid line,  $K = 0.75 \pm 0.04$ . The power-law fit is  $\alpha = 1.06(C_D a L_g)^{-0.50}$ ,  $R^2 = 0.77$

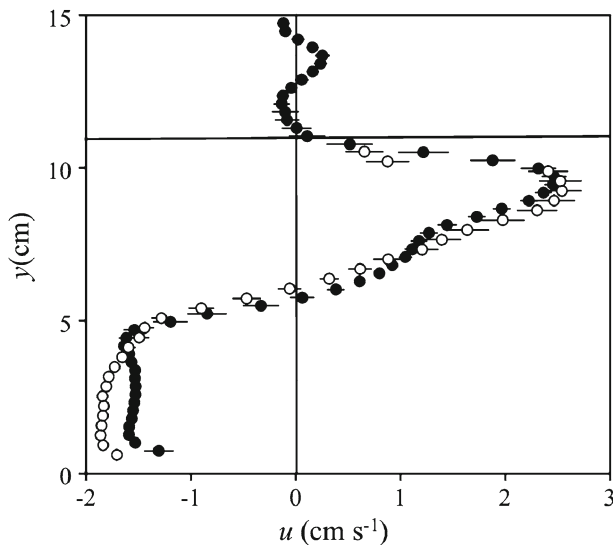


S2,  $\varphi = 1$ ,  $h_3/H = 0.27$ ). The velocity profiles beneath the root layer were nearly identical (Fig. 7). The inflection point observed in case 10 near  $y = 7$  cm is presumably due to the limited time-average, as it cannot be explained by the balance of forces in that region of the flow (pressure, inertia, viscosity).

The model Eq. 18 were solved for the value of  $h_2$  and  $u_2$  that maximized the exchange flow, Eq. 17. The model results are non-dimensional, and must be converted back to dimensional form for comparison to experiments. The model discharge,  $q_{mod}$ , was then calculated using Eq. 16. The high uncertainty in the model prediction (Table 3) is due to the uncertainty in  $g'$ , which is due to uncertainty in the density measurement (Table 1). The model discharge is compared to the two estimates of measured discharge in Table 3. The ratios of the measured and modeled discharge ( $q_{int}/q_{mod}$  and  $q_{16}/q_{mod}$ ) are shown in Fig. 8. The heavy line marks the ratio of 1, corresponding to perfect agreement. First consider the cases that clearly fall in the drag-dominated regime (i.e.  $C_D a L_g > 7$ ), as these cases best fit the model assumptions. For most of these cases the model discharge and the integrated measured discharge ( $q_{int}$ ) agree within uncertainty. The average across the drag-dominated cases is  $q_{int}/q_{mod} = 0.92 \pm 0.12$ . However, the model tends to over predict the integrated discharge ( $q_{int}/q_{mod} \leq 1$ ). This is expected, since viscosity, which would tend to diminish the exchange, was neglected in the model, but its affects are evident in the full velocity profile. In contrast, the measured discharge  $q_{16}$  is based on the measured layer velocities,  $u_1$ ,  $u_2$ ,  $u_3$ , and provides a more direct comparison to the model discharge, which is also based on the layer velocities. Nearly all of the model estimates agree with  $q_{16}$ , within uncertainty, and the average agreement across the drag-dominated cases is  $q_{16}/q_{mod} = 1.06 \pm 0.14$ . Next, consider the two cases not at the drag-dominated limit ( $C_D a L_g < 7$ ). For these cases the model significantly over predicts both measures of discharge ( $C_D a L_g = 4$ ,  $q_{16}/q_{mod} = 0.84, 0.85$ , and  $q_{int}/q_{mod} = 0.67, 0.7$ , Fig. 8). Because these two cases are not in the drag-dominated regime, viscous forces, which are not accounted for in the model, are important. Note that the two cases with low  $C_D a L_g$  produce discharge that is similar in magnitude to the unobstructed exchange flow in the same tank (open circle at  $C_D a L_g = 0$  in Fig. 8). This is consistent with the expectation that for low  $C_D a L_g$  the flow approaches the limit of unobstructed behavior. A similar disparity between observed and theoretical discharge has been observed in other unobstructed lock-exchange studies, and the difference is attributed to viscosity. The theoretical discharge is given by

**Table 3** Comparison of theoretical and measured discharge rate for case 1 to 10

Case	$h'_2$ predicted	$h'_2$ measured	$q$ ( $\text{cm}^2 \text{s}^{-1}$ ) predicted	$q_{int}$ ( $\text{cm}^2 \text{s}^{-1}$ ) measured	$q_{16}$ ( $\text{cm}^2 \text{s}^{-1}$ ) measured
1	0.42	$0.33 \pm 0.03$	$18 \pm 3$	$12.6 \pm 1.7$	$17 \pm 2$
2	0.43	$0.30 \pm 0.02$	$13 \pm 4$	$12.5 \pm 0.5$	$15 \pm 2$
3	0.43	$0.37 \pm 0.03$	$13 \pm 4$	$12.0 \pm 1.8$	$14 \pm 2$
4	0.44	$0.33 \pm 0.02$	$15 \pm 3$	$11.8 \pm 1.4$	$17 \pm 3$
5	0.44	$0.39 \pm 0.05$	$18 \pm 3$	$15.3 \pm 1.6$	$18 \pm 3$
6	0.31	$0.17 \pm 0.05$	$14 \pm 3$	$9.5 \pm 1.2$	$11.8 \pm 1.5$
7	0.32	$0.24 \pm 0.04$	$8 \pm 5$	$7.9 \pm 1.2$	$10 \pm 2$
8	0.33	$0.25 \pm 0.04$	$11 \pm 4$	$10.0 \pm 1.4$	$12 \pm 2$
9	0.33	$0.25 \pm 0.02$	$13 \pm 3$	$11.6 \pm 1.5$	$14 \pm 2$
10	0.34	$0.35 \pm 0.06$	$10 \pm 3$	$10.4 \pm 1.5$	$11 \pm 3$
S1	0.45	$0.40 \pm 0.07$	$17 \pm 3$	$12.8 \pm 1.2$	$12 \pm 3$
S2	0.37	$0.33 \pm 0.03$	$15 \pm 2$	$10.1 \pm 1.0$	$12.3 \pm 1.6$

**Fig. 7** Time-averaged horizontal velocity profile for case 10 (closed circle,  $\phi = 0.15$ ,  $h_3/H = 0.27$ ) and case S2 (open circle, fully blocked,  $h_3/H = 0.27$ ).

Eq. 14, but measured values are depressed near rigid boundaries,  $0.44\sqrt{g'H}$ , and higher near the free surface,  $0.59\sqrt{g'H}$  [17, p. 166].

Floating vegetation in the field typically exists as a belt of vegetation along the shoreline. Ultsch [21] reported temperature difference of  $2^\circ\text{C}$  between water beneath the hyacinth and adjacent open water, which corresponds to  $\Delta\rho = 5 \times 10^{-4} \text{g cm}^{-3}$ . The typical water depth in the shallow band of a lake is approximately 1 m. For floating vegetation with  $\phi = 0.1$  and  $h_3/H = 0.2$ , the model predicts an exchange velocity of  $3 \text{ cm s}^{-1}$  beneath the floating vegetation. During a diurnal cycle, this exchange flow could flush a region of  $O(100 \text{ m})$ . In the Finnis River of Australia, the floating vegetation mat extends 65 m from the bank [8].

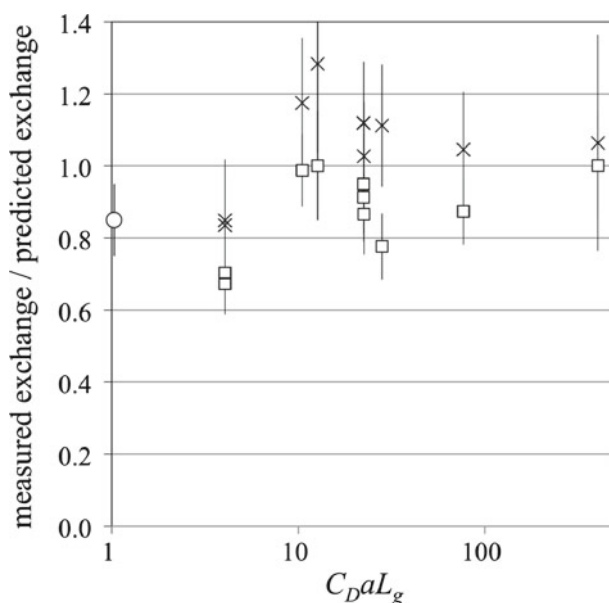


**Fig. 8** Ratio of measured to predicted ( $q_{mod}$ ) exchange flow rate versus  $C_D a L_g$ . Measured flow rate based on Eq. 16,  $q_{16}$  (X). Measured flow rate based on integration of  $u(z)$ ,  $q_{int}$  (square). The unobstructed condition is included for comparison (circle). The average ratios for cases clearly in the drag-dominated regime ( $C_D a L_g > 7$ ), are  $q_{int}/q_{mod} = 0.92 \pm 0.12$  (S.D.) and  $q_{16}/q_{mod} = 1.06 \pm 0.14$  (S.D.), both of which indicate agreement with model predictions, within uncertainty

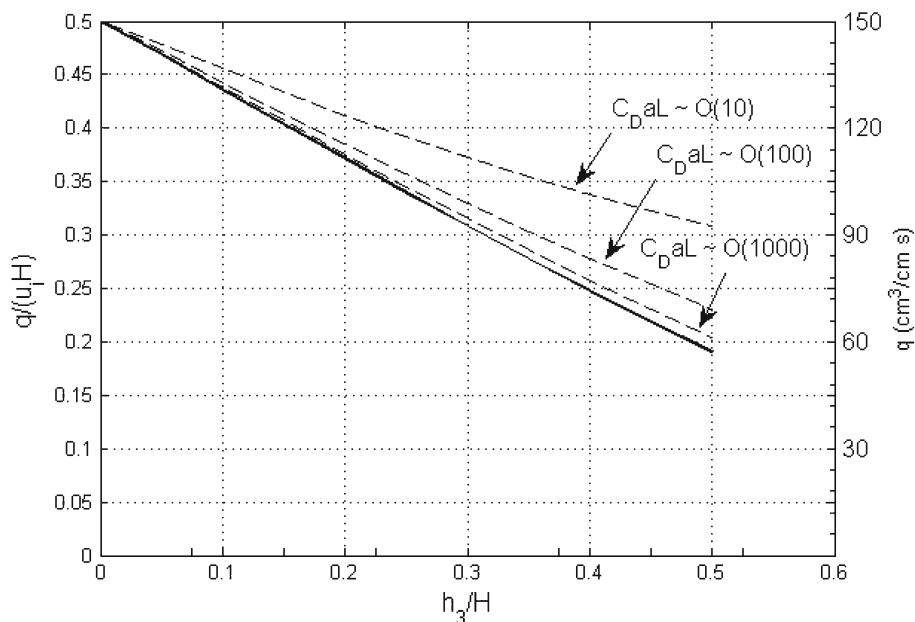


**Fig. 9** Normalized discharge rate  $q/u_i H$  versus fractional penetration depth  $h_3/H$  for different values of  $C_D a L$  (dashed lines). The right axis shows corresponding discharge rate per unit width in  $\text{cm}^3 \text{s}^{-1}$ , for  $\Delta T = 2^\circ\text{C}$  and  $H = 1 \text{ m}$ . The solid line corresponds to a fully-blocked root layer

Similarly, Lovstedt and Bengtsson [11] reported that the width of reed belt in Lake Krankejon in southern Sweden is 40 m. Considering the width of vegetation observed in the field,  $O(10)$  m to  $O(100)$  m, the predicted exchange flow could flush the entire vegetated area each day.

We can use the model to estimate a range of potential discharge for a reasonable range of field parameters. For simplicity, the drag coefficient  $C_D$  is set to 1. The normalized discharge rate,  $q/u_i H$ , is plotted as a function of fraction root depth,  $h_3/H$ , in Fig. 9. Curves for several values of  $C_{Da}L$  are included. As the density of the floating layer ( $a$ ) or the length of the intrusion ( $L$ ) increases, the magnitude of the discharge decreases. For  $C_{Da}L > 100$ , the discharge approaches the condition of a fully block surface layer (solid line in Fig. 9). This is consistent with our observation that the velocity structure for case 10,  $C_{Da}L = 400$ , is nearly identical to the velocity structure with a fully blocked surface layer (Fig. 7). The theoretical curve for the blocked case was computed by setting  $\phi = 1$  and  $\alpha = 0$ . In field applications, the drag coefficient  $C_D$  and the solid volume fraction  $\phi$  of root layer are not easily measured. However, from the above discussions, we expect that the conditions will approach those of a fully blocked layer, i.e. large  $C_{Da}L$ , because the length scales of the intrusion will be large, e.g. from previous paragraph,  $L = 10$ – $100$  m. So, reasonable predictions for field conditions can be made using the fully-blocked curve in Fig. 9.

## 5 Conclusion

Differential heating between regions of open water and adjacent regions of floating vegetation can produce density-driven exchange. The magnitude of exchange depends on the fluid density difference, the root depth and the vegetation drag, parameterized by  $C_{Da}L$ . As the intrusion length-scale ( $L$ ) increases, the flow behavior approaches that of a fully blocked layer, for which the normalized flow depends only on the root depth. A model developed to predict the discharge agreed with measured discharge within uncertainty, for cases in the drag-dominated regime ( $C_{Da}L > 7$ ), which is consistent with the model assumptions. The magnitude of discharge estimated for field conditions suggests that this flow could provide daily flushing of vegetated regions.

**Acknowledgements** This material is based on work supported by the National Science Foundation under grant EAR0509658. Any opinions, findings or recommendations expressed herein are those of the authors and do not necessarily reflect the views of the National Science Foundation.

## References

1. Adams E, Cosler D (1988) Density exchange flow through a slotted curtain. *J Hydraul Res* 26(3):261–273
2. Adams C, Boar R, Hubble D, Gikungu M, Harper D, Hickley P, Tarras-Wahlberg N (2002) The dynamics and ecology of exotic tropical species in floating plant mats: Lake Naivasha, Kenya. *Hydrobiologia* 488(1–3):115–122
3. Azza N, Denny P, van de Koppel J, Kansime F (2006) Floating mats: their occurrence and influence on shoreline distribution of emergent vegetation. *Freshw Biol* 51(7):1286–1297
4. Barr D (1967) Densimetric exchange flows in rectangular channels. *La Houille Blanche* 22:619–631
5. Benjamin T (1968) Gravity currents and related phenomena. *J Fluid Mech* 31:209–248
6. Coates M, Ferris J (1994) The radiatively-driven natural convection beneath a floating plant layer. *Limnol Oceanogr* 39(5):1186–1194
7. Coates M, Patterson JJ (1993) Unsteady natural convection in a cavity with non-uniform absorption of radiation. *J Fluid Mech* 256:133–161
8. Hill R, Webb G, Smith A (1987) Floating vegetation mats on a floodplain billabong in the Northern Territory of Australia. *Hydrobiologia* 150:153–164

9. Jirka G (1979) Supercritical withdrawal from two-layered fluid system—Part 1: two dimensional skimmer wall. *J Hydraul Res* 17(1):43–51
10. Lightbody A, Avenier M, Nepf H (2008) Observations of short-circuiting flow paths within a free-surface wetland in Augusta, Georgia. *Limnol Oceanogr* 53(3):1040–1053
11. Lovstedt C, Bengtsson L (2008) Density-driven current between reed belts and open water in a shallow lake. *Water Resour Res* 44:W10413. doi:[10.1029/2008WR006969](https://doi.org/10.1029/2008WR006969)
12. Mariana M, Mazzeo N, Moss B, Godrigues-Gallego L (2003) The structuring role of free-floating versus submerged plants in a subtropical shallow lake. *Aquat Ecol* 37:377–391
13. Mazda Y, Wolanski E, King B, Sase A, Ohtsuka D, Magi M (1997) Drag forces due to vegetation in mangrove swamps. *Mangroves Salt Marshes* 1:193–199
14. Nepf H (2011) Flow over and through biota. In: Treatise on estuarine and coastal science. In: Wolanski E, McLusky D (eds) Elsevier, San Diego
15. Padial A, Thomaz S, Agostinho A (2009) Effects of structural heterogeneity provided by the floating macrophyte *Eichhornia azurea* on the predation efficiency and habitat use of the small Neotropical fish *Moenkhausia sanctaefilomenae*. *Hydrobiologia* 624:161–170
16. Plew D, Spigel R, Stevens C, Nokes R, Davidson M (2006) Stratified flow interactions with a suspended canopy. *Environ Fluid Mech* 6:519–539
17. Simpson JE (1997) Gravity currents in the environment and the laboratory, 2nd edn. Cambridge University Press, Cambridge
18. Shin J, Dalziel S, Linden P (2004) Gravity currents produced by lock exchange. *J Fluid Mech* 521:1–34
19. Tanino Y, Nepf H (2008) Laboratory investigation of mean drag in a random array of rigid, emergent cylinders. *J Hydr Eng* 134(1):34–41. doi:[10.1061/\(ASCE\)0733-9429\(2008\)134:1\(34\)](https://doi.org/10.1061/(ASCE)0733-9429(2008)134:1(34))
20. Tanino Y, Nepf H, Kulis P (2005) Gravity currents in aquatic canopies. *Water Resour Res* 41:W12402. doi:[10.1029/2005WR004216](https://doi.org/10.1029/2005WR004216)
21. Ultsch G (1973) The effect of water hyacinth (*Eichhornia crassipes*) on the microenvironment of aquatic communities. *Arch Hydrobiol* 72:460–473
22. White FM (1991) Viscous fluid flow, 2nd edn. McGraw-Hill, New York
23. Zhang X, Nepf H (2008) Density driven exchange flow between open water and an aquatic canopy. *Water Resour Res* 44:W08417. doi:[10.1029/2007WR006676](https://doi.org/10.1029/2007WR006676)
24. Zhang X, Nepf H (2009) Thermally-driven exchange flow between open water and an aquatic canopy. *J Fluid Mech* 632:227–243